Journal of Aerosol Science 159 (2022) 105876

Contents lists available at ScienceDirect

Journal of Aerosol Science

journal homepage: www.elsevier.com/locate/jaerosci

Microstructural transition of nanoparticle deposits from multiple dendrites to compact layer

Jeonggeon Kim, Juhwan Shin, Donggeun Lee *

School of Mechanical Engineering, Pusan National University, Busan, 46241, South Korea

ARTICLE INFO

Keywords:
Nanoparticle deposit
Monte Carlo simulation
Dendrites and compact
Microstructural transition

ABSTRACT

Nanoparticle deposit has various microstructures from multiple dendrites to mesoporous compact structures depending on deposition conditions, and the required microstructures are different depending on its applications. There have been recent reports that the overall porosity of deposit can be predicted by a function of diffusive Knudsen number (Kn_D) and dimensionless translational energy (χ_F) of the particle. Unlike compact structures, however, dendritic structures consisting of multiple dendrites cannot be characterized solely by overall porosity and their formation mechanism is not known. In this study, various structures of deposit were produced in a wide range of deposition conditions (Kn_D: $10^{-1.5}$–$10^{1.5}$; χ_F: 10^{-3}–10^{3}) using off-lattice Monte Carlo simulation, and the unique characteristics of the deposit could be visualized by presenting local fractional accumulations of pores as color-filled contours. Furthermore, a spatial autocorrelation was calculated for the contour plot in order to find a quantitative footprint of structural features of nanoparticle deposits, in compact vs dendritic structures. As a result, we successfully identified the dendritic-to-compact structural transition in a quantitative manner, for the first time. Lastly considering the deposition behavior of particles, we developed a new model capable of a priori prediction of the specific deposit structure among compact, dendritic, and transition structures, given the deposition condition in terms of Kn_D and χ_F.

1. Introduction

The deposit layer produced by deposition of aerosol nanoparticles has extremely high porosity, wide specific surface area, and open-porous structure. Due to these structural features, nanoparticle deposits are widely used in various fields such as sensors and catalysts. For example, Castillo et al. (2014) manufactured a highly porous catalytic electrode with a porosity of 95–98% through the deposition of platinum/carbon (Pt/C) nanoparticles, thereby showing a significant increase of specific electric power (from 0.78 to 11.5 kW/g_{Pt}) compared to conventional catalytic electrodes with a porosity of 30%–60% prepared by standard impregnation method. Similarly, there are existing studies that applied nanoparticle deposition of metal oxides, such as tin dioxide or zinc monoxide, for improving the performance of gas sensors (Mädler et al., 2006a; Tricoli et al., 2008) or dye sensitized solar cells (Tricoli et al., 2016). Moreover, nanoparticle deposit can not only increase the reaction sites but also have a great effect on various transport properties (Torquato, 2002, p. 10) such as thermal conductivity (Kovalev & Gusarov, 2017) and permeability (Elmøe et al., 2009), and mechanical properties (Gao et al., 2015), depending on its microstructure. Also, nanoparticle deposition plays an important role in other fields such as filtration (Elmøe et al., 2009; Gao et al., 2020; Kasper et al., 2010), micropatterning (Kim et al., 2006), and ash deposition

* Corresponding author.
E-mail address: donglee@pusan.ac.kr (D. Lee).

https://doi.org/10.1016/j.jaerosci.2021.105876
Received 21 July 2021; Received in revised form 2 September 2021; Accepted 4 September 2021
Available online 22 September 2021

in coal-fired boilers (Kleinhans et al., 2018). Due to the wide applicability, there is a growing technical demand for understanding nanoparticle deposition and a priori prediction of the resulting microstructures for design purpose.

Nanoparticle deposits are often observed as tree-like dendritic structures consisting of multiple individual dendrites with dendritic branches, in addition to well-known porous compact structures. According to Thimsen and Biswas (2007) and Thimsen et al. (2008), nanoparticle deposit produced by flame aerosol synthesis (Strobel & Pratsinis, 2007) has been determined to be composed of a number of tree-like dendrites. These dendritic structures were prepared particularly for the purpose of controlling material properties (Hawkeye & Brett, 2007) such as refractive index (Harris et al., 1984) and wettability (Fan et al., 2004), and for applications such as superhydrophobic surface (Khedir et al., 2017), but the formation mechanism is not clearly revealed. Meanwhile, according to Cherevko and Chung (2011), multi-scale pore structures in which macro pores of tens of micrometers coexist with mesopores of tens of nanometers were beneficial for catalytic performance, presumably due to facile mass transport of reactants through the macro pores and increase of surface area through the mesopores. It is noteworthy that dendritic structures have all of the structural features.

In addition to traditional sintering process, which is vulnerable to large open pores, a smooth-surface compact structure is preferred as a thin film of optoelectronic device for improving the photovoltaic property (Choi et al., 2010; Ortiz et al., 2017). As for the surface coatings, compact structures are required for corrosion protection and better mechanical properties (Hassani-Gangaraj et al., 2015). As such, the required microstructure of nanoparticle deposit varies depending on its application, and thus a priori prediction of the structure from deposition conditions is very important for the process design.

Experimental studies on the structure of the aerosol nanoparticle deposit (Castillo et al., 2014; Mädler, Lall, & Friedlander, 2006; Thimsen & Biswas, 2007; Thimsen et al., 2008; Tricoli et al., 2008, 2016) have been performed under a certain or narrow range of temperature, pressure, and particle size, so it is very difficult to find experimental data covering a wide range of deposition conditions. For this reason, numerical simulations in which deposition conditions are easy to control have alternatively been conducted to investigate the microstructure of formed deposits in detail as follows.

Rodríguez-Perez et al. (2007) presented the density profile along deposition height using on-lattice Monte Carlo (MC) simulation. Castillo et al. (2014) performed a similar MC simulation and showed the mean density of deposit as a function of Peclet number (the ratio of advective transport rate to diffusive transport rate, *Pe*). Li et al. (2009) calculated the local density variation along with the deposit height through on-lattice MC simulation, and expressed the fractal dimension (D_f) (Veerapaneni & Wiesner, 1994) of the deposit as a function of *Pe*. As a result, as *Pe* grew, D_f showed an asymptotic behavior that was initially increased and then leveled off around 3 representing the compact structure. This morphological evolution closely relates to a sort of transition from an open dendritic structure for small *Pe* to compact structures when $Pe \geq 10^{-0.4}$.

Unlike these existing studies that expressed deposition conditions as *Pe* only, Langevin dynamics simulations by Nasiri et al. (2015) or Mädler et al. (2006b) showed that a porosity of nanoparticles' deposit was also decreased to some degree when the size of nanoparticles decreased from 50 nm to 5 nm at a fixed but small value of *Pe*. This suggests that another dimensionless parameter, in addition to *Pe* number, is involved in the size effect of nanoparticles. For the purpose, Stokes number (*Stk*) that was defined with the particle radius as a normalizing length scale has been used as the additional dimensionless variable along with *Pe* (Hunt et al., 2014; Lindquist et al., 2014).

According to Lindquist et al. (2014), the two dimensionless numbers (*Pe*, *Stk*) are not appropriate to represent the operation condition, because the two numbers change simultaneously with gas flow rate and ambient pressure, making it impossible to assess an individual effect of gas pressure or flow rate. Alternatively, they proposed another set of dimensionless parameters: the diffusive Knudsen number (Kn_D, proportional to the particles' mean persistence distance to its radius) and the χ_F defined by the ratio of the particle's translational energy at the advective velocity to the thermal energy. Based on these two dimensionless parameters (Kn_D, χ_F), they presented for the first time a contour map of average packing density of nanoparticle deposit that can be used for a priori prediction of deposit porosity in a wide range of deposition conditions. However, it should also be noted that the predicted local or average porosity does not manifest the presence of dendritic structure and their structural features.

Another notable trend in this area is to analyze pore size distributions of porous structures mostly by numerical simulations (Bhattacharya & Gubbins, 2006; Lee & Hogan, 2021), because pore size distribution has also become a crucial property for the maximal use of nanoparticle deposits under its control. Compared to the existing grid-based atomistic models, Bhattacharya and Gubbins (2006) proposed a new method to greatly shorten the calculation time for pore size distribution of nanoporous materials, and proved that the method is efficient for investigating pore size distributions of several mesoporous model (well ordered) materials. Recently, Lee and Hogan (2021) applied for the first time the foregoing method for nanoparticle deposits with irregular structures and very high porosities, and presented a variety of pore size distributions ranging from unimodal to bimodal. It is however noted that their simulations of nanoparticle deposition were performed on a relatively small domain, mainly under advection dominant conditions where near compact structures are preferentially produced. In fact, bimodal pore size distributions that might be associated with dendritic structure were not observed when depositing spherical nanoparticles, which implies that their deposition condition was not broad enough to cover the entire range of interest, i.e., from dendritic to compact structures. Thus, it is still unclear why and when such dendritic structures are formed.

The objective of this study is therefore to unveil the unique characteristics of dendritic structures in comparison with compact structure upon nanoparticle deposition, to provide a contour plot of the new structural index as a function of Kn_D and χ_F for the first priori prediction of specific deposit structure between dendrite, compact, and intermediate structures from experimental conditions, and finally to develop a new model for understanding what brings the structural difference. For the purpose, off-lattice MC simulation was performed to produce various structures of nanoparticle deposit in a wide range of deposition conditions. Employing a concept of vertical accumulation of local solid or void fraction that will be called 'local porosity distribution', we successfully visualized the

structural difference between the three distinct deposit layers. Then, the spatial autocorrelation was calculated for the local porosity distribution data and displayed with a contour plot against the two dimensionless parameters. As a result, we could identify three specific conditional zones in terms of Kn_D and χ_F, under which dendritic or compact layer is preferentially formed or the compact-to-dendritic structural transition takes place. Finally, a new mathematical model was developed to predict the specific microstructure and/or its transition limit, given a deposition condition. Also, the prediction results were compared with the existing literature data.

2. Off-lattice Monte Carlo simulation

As aforementioned, the two dimensionless parameters, Kn_D and χ_F, are employed in this study as defined in Eqs. (1a) and (1b), respectively. Actually, the two numbers characterize random walks by diffusion and the advective motion by external force of nanoparticles (Lindquist et al., 2014).

$$Kn_D = \frac{l_{mfp}}{r_p} = \frac{\sqrt{m_p k_B T}}{f r_p} \tag{1a}$$

$$\chi_F = \frac{m_p v_{ad}^2}{k_B T} \tag{1b}$$

where l_{mfp} is the mean free path of particles, r_p is the particle radius, m_p is the particle mass, k_B is the Boltzmann constant, T is the temperature of surrounding gas, and v_{ad} is the advective velocity of particles by external force. The friction coefficient f is calculated using Stokes' law and corrected by a slip correction factor C_c (Hinds, 1999, p. 48; Mädler & Friedlander, 2007). The two dimensionless numbers include all the basic factors necessary for the deposition simulation, such as gas properties and physical state, the size and mass of particle to be deposited, and the deposition velocity owing to external force. Also, they have the advantage of separating the influence of pressure and external force (i.e., advective velocity), which are representative operating factors.

Particle behavior in proximity to deposit is characterized by the diffusive motion of the particle due to collision with surrounding gas molecules and its advective motion due to external forces such as thermophoretic or electrostatic force, which can be expressed as Eq. (2) (Kulkarni & Biswas, 2004).

$$\vec{s}(t+\Delta t) = \vec{s}(t) + \vec{l}_{diff} + \vec{l}_{ad} \tag{2}$$

Here, the particle displacement from a position $\vec{s}(t)$ at a time t to the next position $\vec{s}(t+\Delta t)$ is expressed as the vector sum of diffusive displacement ($\vec{l}_{diff}$) and advective displacement ($\vec{l}_{ad}$) for Δt. The $\vec{l}_{ad}$ is calculated as $\vec{v}_{ad}\Delta t$, where the advective velocity ($\vec{v}_{ad}$) is set to be constant given a deposition condition in terms of Kn_D and χ_F, so that the particle moves straight toward the deposition surface. On the other hand, the $\vec{l}_{diff}$ is a random displacement vector of nanoparticle by diffusion and is obtained by generating random numbers in accordance with Gaussian distribution, where each directional component of the vector has a mean value of zero and a standard deviation of $\sqrt{2D\Delta t}$ (Hinds, 1999, p. 111; Moran et al., 2020). Also, the particle diffusivity D is calculated as $k_B T/f$. Based on Eq. (2), nanoparticles are approximated to move toward the deposition plate while making sharp turns in different directions every time step. According to Moran et al. (2020), however, the actual nanoparticles make smooth turns by their inertia, which gives rise to an increase in their persistent distance or the corresponding time step with respect to the case of sharp turn. In this study, the time step Δt is set to three times the conventional particle relaxation time ($\tau_p = m_p/f$) as suggested by Moran et al. (2020). The relevant results will be compared with the results of Langevin dynamic simulation in the literature (Lindquist et al., 2014).

The calculation domain is a rectangular prism with a square bottom having a side of $1000r_p$. When it comes to the coordinate system, x- and y axis are defined on the bottom surface with reference to the origin at a vertex, while the vertical z axis is positive upwards from the origin. Note that all the coordinate axes are nondimensionalized by r_p and marked with asterisk (e.g., $z^* \equiv z/r_p$). Also note that the size of the calculation domain is maintained much larger than (Kulkarni & Biswas, 2004; Mädler et al., 2006b; Nasiri et al., 2015) or similar to (Castillo et al., 2014; Li et al., 2009; Lindquist et al., 2014; Rodríguez-Pérez et al., 2005) the existing simulation studies; this is to avoid numerical artifacts (Nasiri et al., 2015) making the porosity less accurate in case of too small calculation domain and to maintain the fluctuation of the overall porosity below 2% during iterative computations. On the four sidewalls of the calculation domain, a periodic boundary condition is applied.

The present MC calculation was performed in the following order:

A. Create a nanoparticle at a random location on a horizontal x-y plane, $3(\sqrt{2D\Delta t} + l_{ad})$ above the top of the deposit.
B. Calculate the overall displacement vector ($\Delta\vec{s}$) of the particle by Eq. (2): $\Delta\vec{s} = \vec{s}(t+\Delta t) - \vec{s}(t)$.
C. Check if there is any pre-existing deposited particle on the path of $\Delta\vec{s}$; move the original particle to the next location $\vec{s}(t+\Delta t)$ just in case there is no existing particle and return to the process B while updating the particle's position vector; repeat this process until otherwise occurs.
D. If otherwise, meaning that the moving particle collides with the existing particle (or the clean bottom surface) on the path, move the original particle to the contact point and let it stick to the target, and return to the process A.
E. Repeat the foregoing (A-to-D) processes until the total number of deposited particles reaches the target value (6,500,000–24,000,000 depending on the condition).

When it comes to the process A, Nasiri et al. (2015) and Lindquist et al. (2014) fixed the height of creating (or launching) a new nanoparticle at $40r_p$ and $2.1r_p$, respectively, above the top of the deposit. Note that nanoparticle's random walks make the calculation time unacceptably long under highly diffusive conditions (high Kn_D and low χ_F), so one may need to reduce the launching height as long as the resulting microstructure is unaffected. From our preliminary test, we defined the launching height as $N(\sqrt{2D\Delta t}+l_{ad})$ from the top of the deposit, which ensures a similar number of minimum steps required to reach the bottom surface regardless of deposition conditions. With increasing N from 1 to 9, the resulting overall porosity (as well as spatial autocorrelation) was compared in Fig. S1 of supplementary material, indicating that there is no significant N dependence upon $N \geq 3$. Consequently, $N = 3$ was taken and fixed throughout this study.

It is also noteworthy that the abovementioned calculation process is basically a sequence of independent events that launches the next particle after the end of particle deposition, which corresponds to a dilute limit condition in which particles behave independently of each other as described by Lindquist et al. (2014). This condition is common in the field of filtration (Friedlander, 2000, p. 6), which deals with a low number concentration of particles ($<10^5$ # cm^{-3}), and often valid in film deposition of gas-phase reactor where deposition occurs downstream of high-concentration reaction zone. Many literatures (Kubo et al., 2013; Nasiri et al., 2015; Thimsen & Biswas, 2007; Thimsen et al., 2008; Zhang et al., 2012) relating to particle deposition experiments have also confirmed that individual non-agglomerated particles are usually deposited without aggregation prior to deposition.

The contact inspection of a moving particle with existing particles in deposit is a major bottleneck in computation, so only existing particles located within $4r_p$ distance from the trajectory of the moving particle for Δt were considered for the collision detection. Of particular interest is to note that all the aforementioned efforts allowed to perform numerical simulations, similar to those of previous studies using high performance computing (Li et al., 2009; Lindquist et al., 2014), by only single-core operation (Intel 3.3 GHz i7-5820 K processor, 16 GB ram) of personal computers.

The range of the two dimensionless numbers considered in this study is very wide, with $10^{-1.5}$–$10^{1.5}$ for Kn_D and 10^{-3}–10^{3} for χ_F. For example, in the case of TiO_2 particles at 300 K and 1 atm, the particle diameter corresponding to the Kn_D condition spans from 3.8 nm to 1.3 μm. Also under the same condition, metal (Ag, Pt, and Co) particles' diameter lies in a range of ~5 nm–3 μm, and non-metallic particles commonly used in the filtration field, such as plastic, ash, or NaCl, cover a range of ~3 nm–1 μm in diameter. Thus, it is concluded that the current range of the two dimensionless numbers we considered is large enough to cover most particles used in the environment and energy sector.

3. Simulation results

3.1. Validation

The present MC simulations are validated by comparing the results with those of Langevin dynamics simulation in the existing literature (Lindquist et al., 2014). In particular, the existing literature provides a contour plot of packing density of nanoparticle deposits in terms of Kn_D and χ_F, by performing the simulations in a range of $10^{-3} \leq Kn_D \leq 10^{1}$ and $10^{-4} \leq \chi_F \leq 10^{3}$ for a large computational domain ($1000r_p \times 1000r_p$). Note that their overall porosity (= 1 - packaging density) data are extracted from the contour plot and directly compared with those of the present MC simulations in Fig. 1. As a result, our simulation data are well matched with the literature data with a maximum (relative) error of 0.85% and an average error of 0.32% in the present condition ($10^{-1.5} \leq Kn_D \leq 10^{1}$; $10^{-3} \leq \chi_F \leq 10^{2}$).

Meanwhile, the overall or local-average porosity itself might not be able to differentiate between compact vs dendritic structures, because distinctive characteristics of meso and macro pores existing inside and between dendrites can become smeared out in averaging. Also it is very hard to find other experimental indicators that can quantitatively characterize dendrite structures. For further validation, therefore, we performed MC simulations under the same conditions as two literatures (Thimsen & Biswas, 2007; Thimsen et al., 2008) dealing with particle deposition experiments, and compared the overall morphology of as-created deposits with SEM images from the literatures. Fig. 2 shows that the simulated deposit consists of a number of tree-like dendrites, which is quite similar to

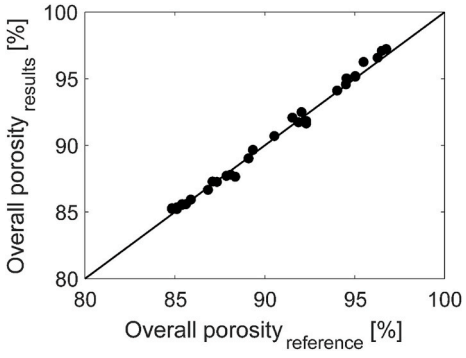

Fig. 1. Comparison of the overall porosity predicted by the present MC simulation with the literature data obtained through Langevin dynamics simulation (Lindquist et al., 2014) under the same deposition conditions.

the SEM image in their height, width, and shape. Note that the MC simulations were stopped when the simulated deposit grew to the height seen on the SEM images.

For reference, according to Thimsen and Biswas (2007) and Thimsen et al. (2008), a flame aerosol reactor was used for formation and deposition of TiO_2 nanoparticles; and the characteristic coalescence time (7.4×10^{-5} ms) of the aerosol particles is much shorter than the characteristic collision time (~0.1 ms), which results in the formation of fully sintered spherical particles prior to their deposition. This implies no further aggregation of the particles until being deposited, which is in proximity of the present dilute limit condition. In order to reproduce the environment for MC simulations as close to the experiment as possible, we collected basic information such as particle size, deposit thickness, and gas and substrate temperature from the literatures; and sequentially calculated the deposit surface temperature, temperature gradients on the surface, and thermophoretic deposition velocity (Hinds, 1999, p. 171) of the particles, referring to Mädler et al. (2006a). The thermophoretic velocity was eventually used as an advective velocity in the present MC simulation.

3.2. Visualization of structural difference of dendrites and compact layer

Previous simulation studies have often presented a S-shaped profile of local porosity in particle deposits along the height from the bottom (Castillo et al., 2014; Kulkarni & Biswas, 2004; Li et al., 2009; Lindquist et al., 2014; Nasiri et al., 2015; Rodríguez-Perez et al., 2007; Rodríguez-Perez et al., 2007, 2007; Veerapaneni & Wiesner, 1994), where the local porosity refers to the average porosity of a (thin) virtual horizontal slice located at a vertical position z^*. Particle deposit layers are divided into bottom, middle, and top layers depending on the local porosity behaviors along the z^* (Castillo et al., 2014; Lindquist et al., 2014). The bottom layer represents the densest but thin layer forming on the deposition substrate, in which the local porosity increases with height ($+z^*$ direction). The middle layer that is connected to the bottom layer occupies most of the particle deposit volume, where the local porosity is almost unchanged with height. The top layer represents the rough top of the deposit, where the porosity increases again from the constant value of the middle layer due to the existence of open surface pores.

It is now recalled that the local porosity, which is basically a horizontal average of void fraction, does not describe the structural characteristics of dendrites. Conversely, we introduced a concept of vertical average porosity in an attempt to visualize the distinct structural features of compact and dendritic layers as follows. As seen in Fig. 3, the middle layer of the deposit completed by MC simulation is cut to a thick slice with a certain height ($\Delta z^* = 100$) and then divided into a large number of (virtual) vertical rectangular prisms. Since each prism was set to have a square top and bottom with a side length equal to the particle diameter ($\Delta x^* = \Delta y^* = 2$), the middle layer slice becomes 500×500 individual vertical prisms. Here, the void fraction (i.e., the vertical average porosity) within each prism is calculated at the position of the prism, and then displayed with different colors on the entire top surface of the middle layer. As such, the projection image of vertical porosities can visualize the distinctive structural features of deposits with a color-filled contour plot (see Fig. 3; hereinafter referred to as "local porosity distribution (contour)").

There is an issue with determining the height Δz^* of the middle layer slice. If the Δz^* is too large, particles belonging to different branches could be involved in the porosity calculation for a single prism, which causes a smoothing of the internal structure of

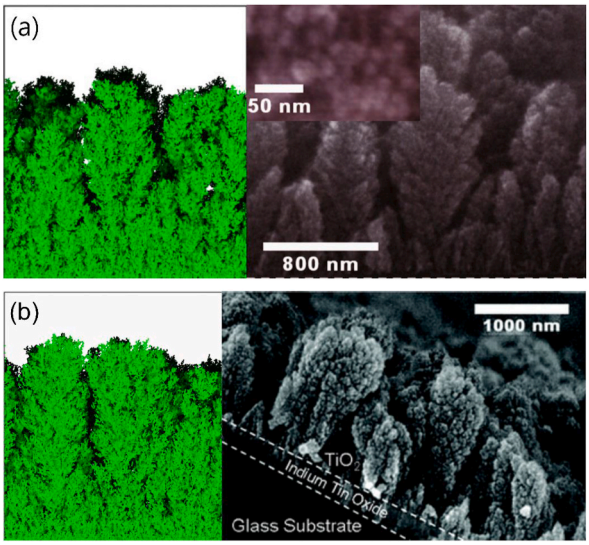

Fig. 2. A comparison of the overall morphology of simulated deposits with SEM image in the literatures; the experimental conditions are (a) $\log(Kn_D) = 1.7$, $\log(\chi_F) = -1.6$ (Thimsen & Biswas, 2007) (b) $\log(Kn_D) = 1.5$, $\log(\chi_F) = -0.6$ (Thimsen et al., 2008) (adapted from Thimsen and Biswas (2007) with permission of Wiley–Blackwell and adapted from Thimsen et al. (2008) with permission of American Chemical Society); in the simulation image, dendrites in the back are highlighted with a dark color. (For interpretation of the references to color in this figure legend, the reader is referred to the Web version of this article.)

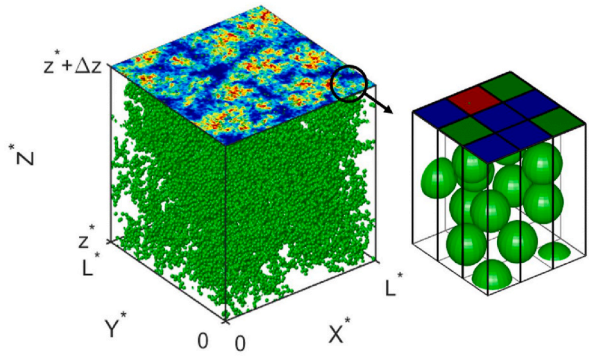

Fig. 3. A conceptual diagram illustrating how to set up virtual vertical prisms and to visualize the local porosity data together with an example of local porosity contour.

dendrites by excessive averaging. Given a too-thin slice, on the other hand, it does not represent the three-dimensional structure of the dendrites, so the identification of dendrite itself becomes impossible. Hence, a set of preliminary simulation with three different values of Δz^* was implemented to prove the two limiting cases. Fig. S2 of supplementary material shows that there seems no significant difference in the local porosity contours while changing Δz^* from 10 to 100 and 200; however, in the case of $\Delta z^* = 10$, some of branches that are parts of a dendrite could be seen separated from its stem in Fig. S2(a), being identified as another dendrites; whereas, with $\Delta z^* = 200$, the internal structure and boundary of dendrites in Fig. S2(c) are clearly blurred as compared with Fig. S2(b) of $\Delta z^* = 100$. Consequently, the height of the prism will be fixed at $\Delta z^* = 100$ hereafter.

Fig. 4 shows the three contour plots of the local porosity distribution of deposits produced under different deposition conditions; referring to the color scale, the red represents an area where particles are closely packed with a porosity of less than 80%, while the

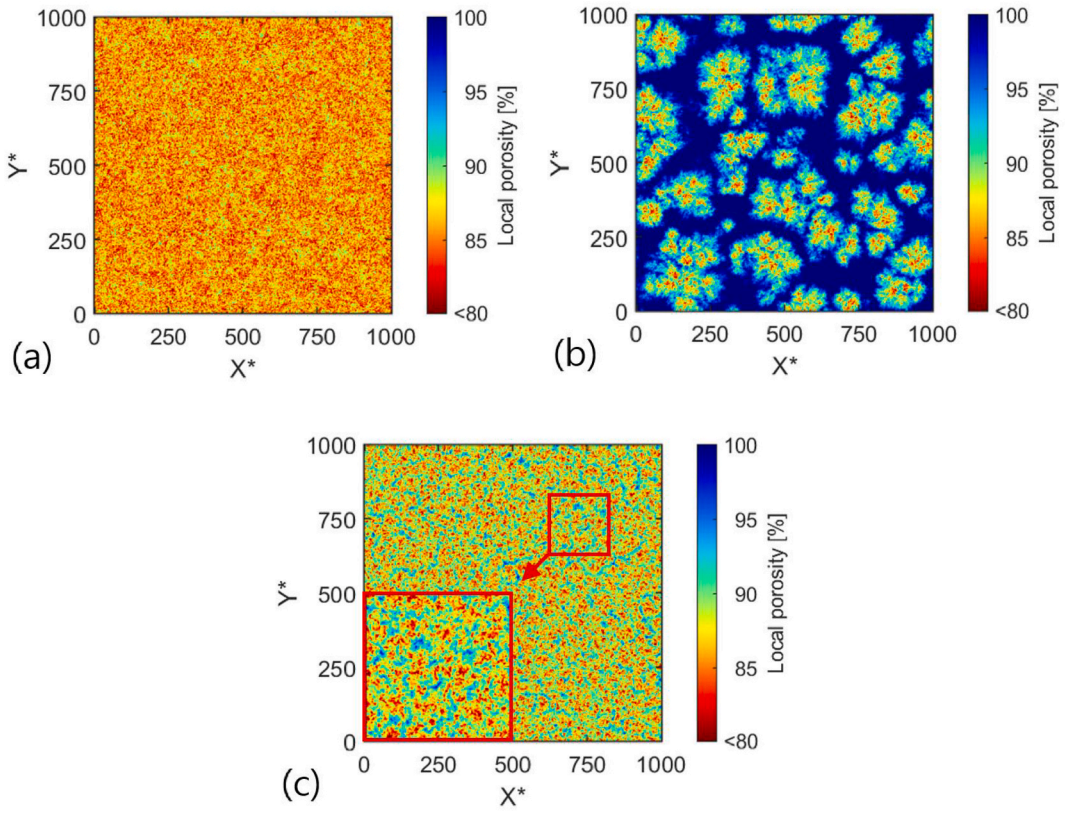

Fig. 4. Local porosity contour plots of deposit structures with identification of the structures such as (a) Compact structure ($I = 0.23$) under $\log(Kn_D) = 0$ and $\log(\chi_F) = 2$; (b) Dendritic structure ($I = 0.90$) under $\log(Kn_D) = 1$ and $\log(\chi_F) = -2$; and (c) Intermediate structure ($I = 0.53$) under $\log(Kn_D) = 1$ and $\log(\chi_F) = 0$. The inset of (c) is a magnified image of red-square area ($200r_p \times 200r_p$). (For interpretation of the references to color in this figure legend, the reader is referred to the Web version of this article.)

blue represents an empty area in which there are few particles with a porosity of close to 100%. From the figure, one may intuitively notice the structural differences between dendritic and compact structures. Specifically, in Fig. 4(a), where the advection is dominant, the red dots are randomly distributed over the entire area, so the overall porosity is also low. This proves that it is the compact structure. In contrast, Fig. 4(b), which is the case of strong particle diffusion, is seen as if there are many individual islands on the sea. In fact, the island is a single dendrite and a dendritic structure comprises multiple dendrites. Measuring the distance between dendrites and the width of a dendrite allows to further explore the structural characteristics of dendrites in a quantitative manner. Fig. 4(c) shows an interesting structural pattern of deposit obtained in the middle of the two extreme conditions, where neither the diffusion nor the advection is dominating. Overall, the deposit layer looks like a near compact structure where small red lumps (but larger than the red dots in Fig. 4(a)) are randomly and closely deposited. However, a closer look as in the presented inset reveals that the deposit layer also has the structural feature of tiny dendrites. In particular, as the deposition condition changes from diffusion-dominant to advection-dominant to some degree, i.e., from Fig. 4(b) to Fig. 4(c), the individual large dendrites clearly get smaller in size and closer to each other in mutual distance. This morphology change is further progressed up to the compact structure in Fig. 4(a) with increasing advection velocity; apparently, the small dendrites seen in Fig. 4(c) seem to break up into tiny particles and fill the void spaces with the particles.

3.3. Overall porosity and autocorrelation map

In this section, we present a process of quantifying the structural characteristics of the deposit observed in the previous section. The spatial autocorrelation index, also known as Moran's index (I) (Moran, 1950), is one of the indicators in statistics designed to evaluate the spatial distribution of a given variable or the extent of being clustered (correlated). In the case of randomly dispersed, the index I becomes zero, which represents the spatial randomness or independence of the dispersed particles. On the contrary, the closer the index I is to $+1$, the more similar (highly correlated) regions are clustered, indicating that it is easy to discriminate them by neighborhood similarity (Zhang & Lin, 2007).

We calculated spatial autocorrelation index for the local porosity distribution data seen in Fig. 4, in accordance with the calculation process described in Appendix. As a result, I values are 0.23, 0.90, and 0.53 for the compact, dendritic, and intermediate structures of Fig. 4(a), (b), and 4(c), respectively. It is notable that the I values vary depending on the structures exactly as stated above, suggesting that the index I is likely used as an appropriate indicator for identifying the structure of particle deposits. Here, it should also be noted that there is an issue with no distinct criterion on how to define the transition boundary of the three structures.

For this issue, we first divided each range of χ_F and Kn_D into 7 different bins that are equally spaced in log scale, which created 49 different cases in total (see the symbols in Fig. 5); and then repeatedly performed the MC simulation followed by the post processing to yield the I values for the entire cases. The results show that the index I varies from 0.22 to 0.93 under the whole deposition conditions.

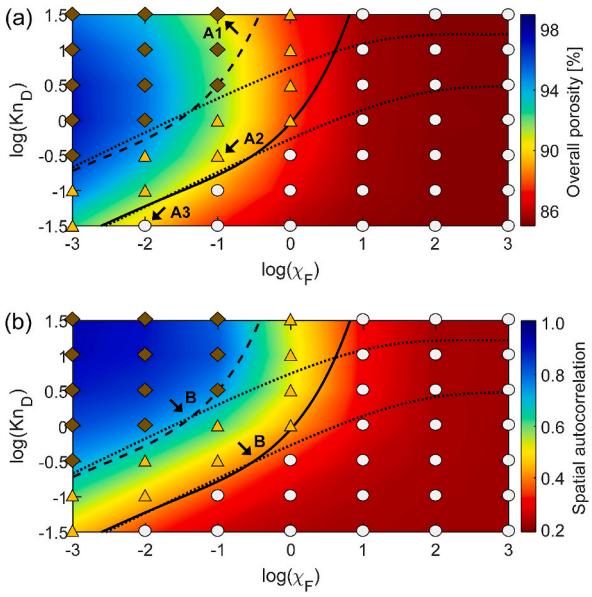

Fig. 5. A graphical guidance of microstructural evolution of nanoparticle deposits with (a) the overall porosity contour and (b) spatial autocorrelation index contour plotted as a function of $\log(\chi_F)$ and $\log(Kn_D)$; A diamond (◆) represents a dendritic structure, circle (○) represents a compact structure, and triangle (▲) represents an intermediate structure between the two. Upper and lower dotted lines (···) represent the transition boundaries predicted by the first model Eq. (10) toward dendritic and compact structures, respectively. Solid line (−) and dashed line (- -) are the predicted transition boundaries by the modified model equation, connecting the points having equal value of index I, i.e., $I = 0.4$ and $I = 0.7$, respectively; Arrows A1, A2 and A3 indicate that three distinct structures can be formed even with a similar overall porosity. Arrow B represents the point where the discrepancy between Eq. (10) and Eq. (14) begins.

Based on 49 image sets of local porosity contour and the front view of deposit (such as Figs. 4 and 2, respectively), a comparative analysis was undertaken to group the I values for specific cases that can be no doubt classified as dendrite or compact structure. As a result, the cases of $I > 0.7$ safely result in dendritic structures, while the cases of $I < 0.4$ show compact structures. In the case of $0.4 \leq I \leq 0.7$, the resulting structure is hard to identify between dendrite and compact, just like in Fig. 4(c), so it was named as an intermediate structure denoting the structural transition.

In Fig. 5(a) and (b), the overall porosity contour and spatial autocorrelation index contour are respectively plotted as a function of $\log(\chi_F)$ and $\log(Kn_D)$, wherein the three symbols signifying the three distinct deposit structures are overlaid on the contour plots: diamond (◆) represents a dendritic structure; circle (○) represents a compact structure; and triangle (▲) represents an intermediate structure between the two. When it comes to the overall porosity contour in Fig. 5(a), the lower the χ_F and/or the higher the Kn_D, the overall porosity tends to increase (to the blue). When the condition becomes advection-dominant moving toward the lower right corner, the overall porosity tends to decrease (to the red). As an exception, under diffusion-dominant conditions with $\log(\chi_F) \leq 0$ and $\log(Kn_D) \geq 0.5$, the overall porosity begins to slightly decrease with further increase of $\log(Kn_D)$, which was attributed to the strengthened random ballistic motion of tiny nanoparticles by Lindquist et al. (2014).

Of particular interest is to find diamond symbols only in the upper left corner of Fig. 5(a) encompassing blue to pale green, suggesting that dendrites are favored to form under diffusion-dominant conditions. Consistently, the corresponding region in Fig. 5(b) is blue, indicating that $I > 0.7$, and its boundary was marked with a dashed line. On the contrary, as the condition becomes more advection-dominant (moving to the right with increase of χ_F), the color in Fig. 5(b) gradually changes toward red with continuous decrease of the index I. This signifies a gradual recovery of randomness of particle depositions and its preferential formation of compact structure as well. In the figure, the left boundary of circles (compact structures) was marked with a solid line. Naturally the region in between the dashed and solid lines represents the structural transition zone as confirmed with triangles.

Overall, the index I shows a pretty similar behavior to the overall porosity along with variations of χ_F and Kn_D. However, recalling the aforementioned exceptional behavior of the overall porosity under high Kn_D and low χ_F conditions, the index I is not likely subject to the abnormal effect of highly diffusive nanoparticles. More specifically, the overall porosities at the three points marked by the arrows A1, A2, and A3 in Fig. 5(a) are 90.5%, 90.7%, and 89.7%, respectively, showing the yellow color all together. But the symbol or morphology of deposits significantly changes from diamond (dendrites) to circle (compact structure) in Fig. 5(a) together with a great color change of index I in Fig. 5(b) (from blue to red through brown; corresponding to the value change of I from 0.80 to 0.33 through 0.45, respectively). This again proves that the overall porosity does not describe the structural difference of particle deposits.

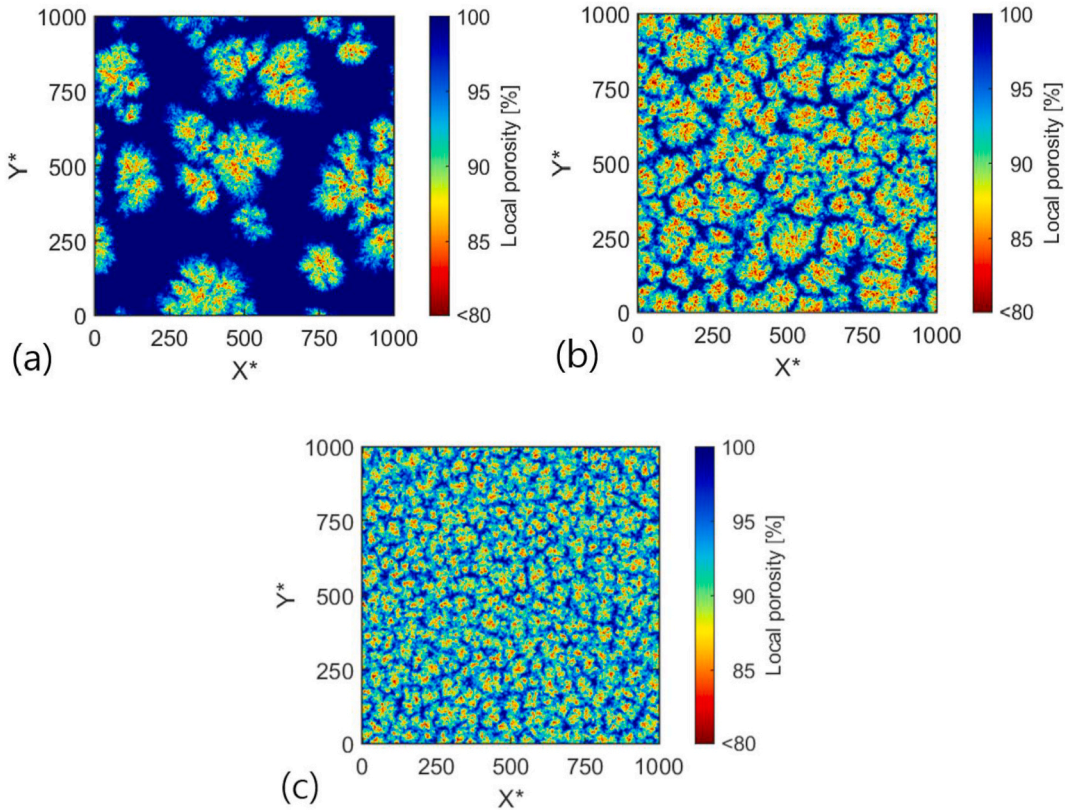

Fig. 6. Distinctive morphological evolution of multiple dendrites toward the compact structure by increasing χ_F or decreasing Kn_D: (a) $\log(Kn_D) = 1, \log(\chi_F) = -3, I = 0.92, \Theta_p = 96\%$; (b) $\log(Kn_D) = 1, \log(\chi_F) = -1, I = 0.82, \Theta_p = 91\%$; and (c) $\log(Kn_D) = 0.5, \log(\chi_F) = -1, I = 0.75, \Theta_p = 91\%$, where Θ_p is overall porosity.

Furthermore, it is interesting to know how individual dendrites behave in response to the variation of each parameter (χ_F vs Kn_D), particularly within the diffusion-dominant regime. Referring to Fig. 5(a), we considered two distinct paths for the purpose: 1) $-3 \leq \log(\chi_F) \leq 1$ at $\log(Kn_D) = 1$, and 2) $-1 \leq \log(Kn_D) \leq 0.5$ at $\log(\chi_F) = -1$. The results are summarized with three representative contour plots in Fig. 6, with focus on the dendrites' behavior.

When $\log(\chi_F)$ alone increases from -3 to -1 along the first path, large dendrites widely separated in Fig. 6(a) are converted into smaller dendrites with narrow interspace in Fig. 6(b). At this moment, the index I slightly decreases from 0.92 to 0.82, still in the dendrite-appearance zone ($I > 0.7$), while the overall porosity clearly decreases along with a significant decrease in area fraction of blue (empty) space. Further increase in $\log(\chi_F)$ makes this trend more prominent by making the index I fall down below the first transition boundary ($I < 0.7$), and eventually reaches a minimum of $I = 0.2$ by showing the compact structure. A similar early-stage behavior of dendrites has been observed by decreasing $\log(Kn_D)$ from 1.0 in Fig. 6(b) to 0.5 in Fig. 6(c) at $\log(\chi_F) = -1$ along the second path. Again, further decrease of $\log(Kn_D)$ alone leads to the aforementioned morphological transition toward the compact structure.

To sum up the above results, dendritic structure is first transformed into an intermediate structure with the decrease in Kn_D and the increase in χ_F. In this process, dendrites are reduced in size and interspacing, leaving only traces of the empty space between dendrites and almost filling it up like Fig. 4(c). After that, this structural change is continued but slowed down until reaching the compact structure. A more detailed process of change is included in Fig. S3 of supplementary material; Fig. S3(a)–(e) present the five local porosity contours obtained while the χ_F increases along the first path; whereas Fig. S3(f)–(i) show the effect of Kn_D on the morphology of deposits along the second path.

4. Model development

4.1. Model description

This chapter is devoted to how to develop a new model capable of a priori prediction of deposit structures in compact vs dendrites. As a first step, we investigated the difference in morphological evolution of deposits growing under the two extreme conditions. A two-dimensional MC simulation was performed for an intuitive understanding of the difference. Fig. 7(a) and (c) represent the deposit structures at the early and late stages of growth, respectively, under a diffusion-dominant condition; both figures were directly compared with Fig. 7(b) and (d) for an advection-dominant case, respectively. In the early stage of growth, there is no remarkable difference in deposit structures; Fig. 7(a) and (b) show almost identical structures where particles are randomly deposited irrespective of deposition condition, leaving many small isolated protrusions like a sprout on the floor. However, their growth patterns are quite different depending on the deposition condition. Under the highly diffusive condition, some of the early protrusions selectively grow to multiple tree-like dendrites (compare Fig. 7(a) and (c)). Note that initially unoccupied parts on the floor remain clean (undeposited) during the growth. In contrast, under the advective condition, particle deposition seems to randomly occur on the entire floor without site preference, so that the deposit uniformly grows to a near compact layer.

Here, we focused on the fact that dendrites grew only from existing protrusions on the surface. Once small protrusions are generated by chance on the floor as seen in the inset of Fig. 7(a), a next (released) particle, if subject to random walks by diffusion, will have a much greater chance of colliding with the protrusions due to the predominant horizontal displacement (see Eq. (2) and its relevant statements in Chap. 2). As such, the selected protrusions fast grow to be tall and thick under diffusion-dominant condition. As this process continues, the thickening of protrusions would decrease the surface-to-surface distance between adjacent protrusions so that significantly reduces the number of particles arriving at the remaining clean floor.

Another point to note is about deposition fluxes of particles on to the top and side wall of protrusions, because the flux (per unit

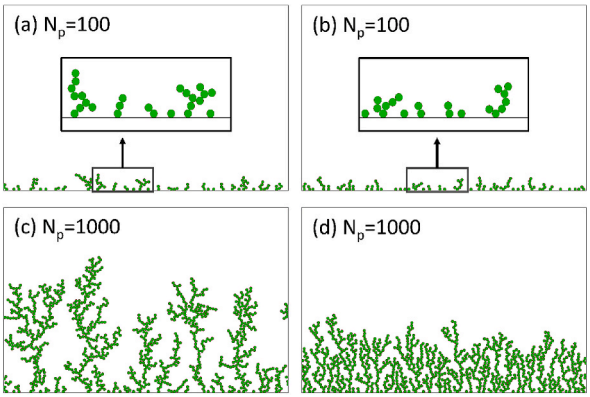

Fig. 7. Similarity and Dissimilarity at the early and late stages in the growth process of nanoparticle deposits: for simplicity, MC simulation was performed on a smaller 2-D calculation domain of $200r_p$; and N_p stands for total number of deposited particles in the two-dimensional deposition; (a) $Kn_D = 2, \chi_F = 0.0025, N_p = 100$; (b) $Kn_D = 0.2, \chi_F = 1600, N_p = 100$; (c) $Kn_D = 2, \chi_F = 0.0025, N_p = 1000$; and (d) $Kn_D = 0.2, \chi_F = 1600, N_p = 1000$.

area) directly determines the increasing rate of height or width of dendrites. Given a constant rate of deposition toward any surface of dendrite (relating to the random motion of particles), the deposition flux to the side wall is rather decreased by the increase of side-wall area during the growth, plus further decreased by the aforementioned shadowing effect. Hence the increase in the width of dendrite is slowed and eventually stopped, while the top can grow actively with no limitation. This speculation is deemed as a plausible explanation to the appearance of isolated dendrites in Figs. 4 and 6. In contrast, highly advective deposition is relatively simple to understand. Since particles move straight down to the floor starting at random positions, they must be equally deposited without discriminating the top of existing dendrites and clean floor, leading to the random simultaneous growth of deposits.

4.2. Formulation of model equation

Based on the foregoing speculation, we developed a predictive model of the deposit structure as follows. Recalling the inset of Fig. 7 (a), early-stage dendrites are approximated to rectangular columns with height H and width w, and these columns are simplified by arranging them periodically by interval L. Fig. 8 shows a schematic diagram describing the behavior of a nanoparticle in between two adjacent columns (shown as shaded rectangles); Region A refers to the top of the column, Region B refers to the side wall of the column, and Region C refers to the unoccupied clean floor.

The probability that particles are deposited to Region A is called $P_{dep,0}$, and the number of particles deposited to the A is $NP_{dep,0}$ when N particles in total pass through a virtual dotted line located at height H. Here, $N(1-P_{dep,0})$ is the number of non-deposited particles entering the void space between the columns. Then, the survived particles exhibit consecutive random walks by diffusion over time while keep moving downward as depicted by a dashed arrow in Fig. 8. Some of these survived particles are deposited to Region B of the side, until the rest particles reach Region C. When the average probability of particles being attached to Region B during the time step Δt is P_{dep}, the number of particles deposited to Region B for Δt immediately after passing through the horizontal (dotted) plane is $N(1-P_{dep,0})P_{dep}$, which in turn yields the number of still non-deposited particles as $N(1-P_{dep,0})(1-P_{dep})$. After the second time step $t = 2\Delta t$, the number of non-deposited particles is likewise calculated by $N(1-P_{dep,0})(1-P_{dep})^2$. As such, the number of survived particles per each consecutive time step is continually decreasing with the number of steps by the subsequent side-wall depositions. If m steps are required to reach Region C, the number of particles deposited to Region C is $N(1-P_{dep,0})(1-P_{dep})^m$. Here, the total number of steps m is simply determined by the advective velocity (v_{ad}) and the height (H) as $m = H/v_{ad}\Delta t$, not being affected by the diffusive motion with an average displacement of zero in the z direction.

Overall, if the particle flux to the clean floor (Region C) is much lower than that to the top (A) or side (B) of column, most of incoming particles will be used for the protrusions (columns) to grow to dendrites. This is expressed as the inequality in Eq. (3), where S_A and S_C are the areas of Region A and Region C, respectively, and the left and right terms can be considered as the particle flux to the regions.

$$\frac{NP_{dep,0}}{S_A} \gg \frac{N(1-P_{dep,0})(1-P_{dep})^m}{S_C} \tag{3}$$

When it comes to the probability of being deposited to Region A, it is calculated simply by the area ratio as $P_{dep,0} = S_A/(S_A+S_C)$, because all particles pass through the virtual horizontal plane (the dotted line in Fig. 8) with the same probability due to the random nature. Applying this to Eq. (3), the inequality equation is further simplified into Eq. (4).

$$1 \gg (1-P_{dep})^m \tag{4}$$

The right side of Eq. (4) rapidly decreases in the direction that satisfies this inequality, when P_{dep} is increased by the transverse

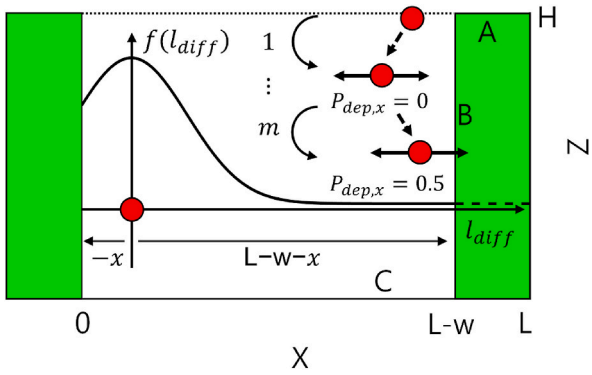

Fig. 8. A schematic diagram of particle behavior in between two adjacent dendrites (modelled as columns); where 'A', 'B', and 'C' signify the top end, side wall of the column, and the clean floor, respectively; the numerical value of 1-to-m illustrates m-times repeated advective motion of particle until reaches the floor; the relative coordinate x was defined as depicted and used only for deriving Eq. (12) while the absolute coordinate (written as 'X') was defined from the side wall of the left column and used for Eqs. (7,13); and the shaded (green) rectangles stand for two modelled dendrites. (For interpretation of the references to color in this figure legend, the reader is referred to the Web version of this article.)

(diffusive) movements of the particles at higher Kn_D or the number of moving steps (m) is increased with decreasing χ_F. Thus, dendritic structures will be predominantly created. In the opposite cases such as lowering Kn_D or increasing χ_F, both P_{dep} and m decreases, so that the right-side term of Eq. (4) increases to approach unity. At this moment, the deposit layer will be near compact. In summary, since the two predicted structures are exactly consistent with the simulation results in Chap. 3, Eq. (4) is deemed appropriate as a conditional criterion for determining the deposit structures.

Moreover, the comparative code "≫" is intended to emphasize that the right-side term in Eq. (4) must be sufficiently small to produce a definite dendritic structure, considering that there is a transition zone in between dendrites and compact structure (see Fig. 5). Here, it is ambiguous how small the right-side term of Eq. (4) should be. In Chap. 3, either $I = 0.4$ or 0.7 was presented as a boundary value on the map for compact or dendritic structure, respectively. Similarly, we introduce a critical probability, P_c, which acts as an upper threshold for the appearance of dendrites structure as seen in Eq. (5). Note that the P_c will be included as a fitting parameter of the model equation, but not being explicitly involved in the following formulation process.

$$P_c = \left(1 - P_{dep}\right)^m \tag{5}$$

The next step is to formulate the P_{dep} accounting for the particle behavior depicted by dashed arrows in Fig. 8. For simplicity, we approximated that particle's behavior is two dimensional (2D) on the x-z plane; the horizontal ($x-$) component of displacement vector of a particle for Δt is $\pm\sqrt{6}l_{mfp}$ ($=\sqrt{2D\Delta t}$) only by diffusion, while its vertical displacement is simply $l_{ad}(=v_{ad}\Delta t)$ to the negative z direction only by advection, recalling no net displacement by diffusion on average. Note that a particle, if located at x within a distance of the horizontal displacement from Region B as $x \le \sqrt{6}l_{mfp}$, can be deposited to Region B with a probability of 0.5. On the other hand, particles if $x > \sqrt{6}l_{mfp}$ will not be deposited to the wall of column, moving to the next step. As such, the local deposition probability $P_{dep,x}$ of particles, which is basically a function of the distance (x) from the side wall of the column, can be expressed as Eq. (6) and represented as a solid line in Fig. 9(a).

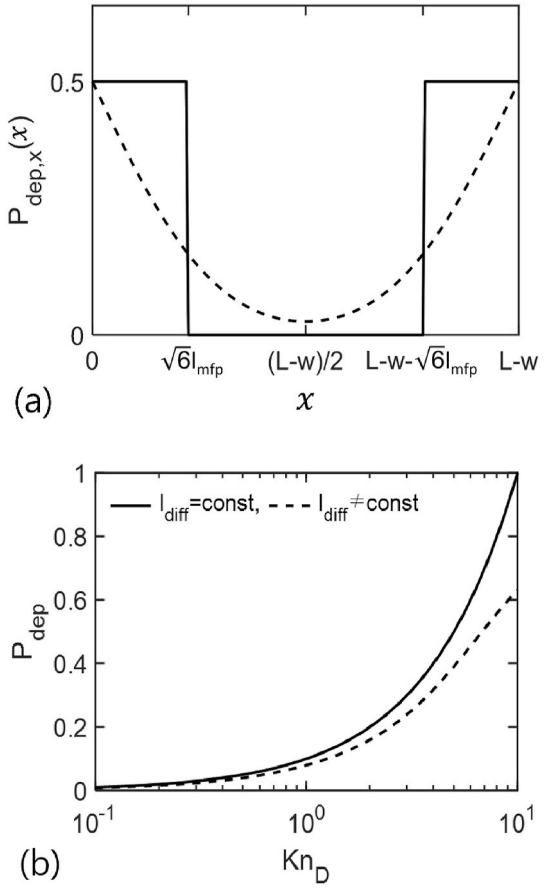

Fig. 9. Functional behaviors of (a) local deposition probability $P_{dep,x}$ and (b) average deposition probability P_{dep} along the distance x from the side wall of left column; where the stepwise profile implies that all particles are subject to an equal (constant) diffusive displacement, while the continuous (dashed) curves represent the results for normal probability distribution.

$$P_{dep,x}(x) = \begin{cases} 0.5, & 0 < x \le \sqrt{6} l_{mfp} \\ 0, & x > \sqrt{6} l_{mfp} \end{cases} \tag{6}$$

Averaging $P_{dep,x}(x)$ over the wall-to-wall distance $(L - w)$ between dendrites, the average probability P_{dep} can be expressed in terms of l_{mfp} or Kn_D as

$$P_{dep} = \frac{1}{L-w} \int_0^{L-w} P_{dep,x}(x) dx = \frac{\sqrt{6} l_{mfp}}{L-w} = \frac{\sqrt{6} Kn_D}{L^* - w^*}. \tag{7}$$

Let us recall that the number of discretized steps m was determined from the height H of the dendrite and the advective velocity v_{ad} as seen in Eq. (8), where $\Delta t_{z,av}$ is the residence time of particle until being deposited to the floor.

$$H \,/\, v_{ad} = \Delta t_{z,av} \cong m \Delta t \tag{8}$$

It is noteworthy that the value of m should be large enough to ensure near-zero statistical average for vertical diffusive displacements of particle. If otherwise, vertical random walks of particle may alter the actual vertical velocity from v_{ad} as well as the m. In order to secure a sufficiently large value of m regardless of deposition conditions, we revisited functional variations of $\Delta t (= 3\tau_p)$, l_{mfp}, and m with decreasing r_p at a fixed v_{ad} toward the diffusion-dominant condition. Although the relaxation time τ_p (or Δt) is shortened with decrease of r_p under the free-molecular regime by its definition $\tau_p = m_p / f \propto r_p / C_c \propto r_p^2$), the random walk velocity defined as $\sqrt{k_B T / m_p}$ more increases in proportion to $r_p^{-3/2}$, which in turn increases the particle's persistent distance l_{mfp} for each time step. Hence, if the H is fixed constant and not so large, the m can be decreased to below the lower limit by $m \propto H / l_{mfp}$. In order to circumvent this potential problem, the H is set to increase in proportion to the increase of l_{mfp}. Applying $H = C l_{mfp}$ (where C is a proportional constant) to Eq. (8), a secured limit of m can be determined solely from the χ_F, independent of Kn_D as

$$m = \frac{C l_{mfp}}{v_{ad} \Delta t} = \frac{C}{3 v_{ad}} \sqrt{\frac{k_B T}{m_p}} = \frac{C}{3} \chi_F^{-0.5} \tag{9}$$

Substituting Eqs. (7) and (9) to the terms of P_{dep} and m in Eq. (5) and taking a natural logarithm on both sides, we obtained a first model equation expressed in terms of the two dimensionless parameters as

$$\chi_F^{0.5} = C_1' \ln\left(1 - C_2' Kn_D\right) \tag{10}$$

where C_1' and C_2' are unknown constants that will be obtained by curve fitting to pass the points corresponding to the boundary of structural changes ($I = 0.4$ or 0.7) in Fig. 5(b). The values are listed in Table 1 and P_c in Eq. (5) was included in C_1'. Thus, Eq. (10) indicates the functional relationship of χ_F and Kn_D, which represents the boundary of structural changes passing through $I = 0.4$ or 0.7 depending on the set of C_1' and C_2' used. The two boundary curves are plotted as dotted lines in Fig. 5 such that the upper dotted line represents the dendrite-to-intermediate transition boundary while the lower dotted line indicates the intermediate-to-compact transition. In Fig. 5(b), however, the upper line can trace the real boundary between "blue" and "green" up until the point B from the left, i.e., only in a range of $\log Kn_D \le 1$, and the lower line is working likewise in a range of $\log Kn_D \le -0.5$. Beyond the limit, the both lines can no longer be used for prediction.

To improve the model prediction accuracy in high Kn_D, the expression of local deposition probability $P_{dep,x}(x)$ is modified to involve Gaussian distribution of diffusive displacements, which is closer to the reality than the foregoing assumption that all particles have a fixed diffusive displacement.

$$f\left(l_{diff}\right) = \frac{1}{\sqrt{2\pi\sigma^2}} \exp\left(-\frac{l_{diff}^2}{2\sigma^2}\right) \tag{11}$$

Equation (11) is a probability density function for Gaussian random displacements (l_{diff}) with a standard deviation (σ) of $\sqrt{2D\Delta t}$ ($= \sqrt{6} l_{mfp}$) and an average of zero. Note that the l_{diff} is actually a diffusive displacement that can vary from -∞ to +∞ depending on the moving direction. Provided that a particle is located $+x$ away from the left-column surface, it might be more convenient to use a relative coordinate with reference to the center of the particle, as conceptually depicted with x in Fig. 8. The probability for the particle to be deposited on the right-side wall of the left column $P_{dep,x}(x)$ is obtained by subtracting the probability $P_{sur,x}(x)$ for the particle to

Table 1
Collection of the whole coefficients in Eqs. (10,14-17) for model prediction of microstructural transition boundaries of nanoparticle.

	C_1'	C_2'	C_1''	C_2''	C_1	C_2	C_3
Case 1[a]	−5.10	0.33	−0.44	0.17	0.10	2.27	0.68
Case 2[b]	−2.44	0.06	−0.13	0.50	0.28	7.69	6.82

[a] From compact structure to intermediate structure.
[b] From dendritic structure to intermediate structure.

survive (not to be deposited) over the displacement for Δt from unity. Here, the $P_{sur,x}(x)$ is the same as the probability for the particle to horizontally move as much as ($-x$ to $L-w-x$) in terms of l_{diff} from the original position (see Fig. 8). Thus the $P_{dep,x}(x)$ can be expressed as

$$P_{dep,x}(x) = 1 - \int_{-x}^{L-w-x} f\left(l_{diff}\right) dl_{diff} \tag{12}$$

Now, the average deposition probability P_{dep} during Δt is calculated by averaging $P_{dep,x}(x)$ over the empty space between adjacent columns as

$$P_{dep} = \frac{1}{L-w}\int_{0}^{L-w} P_{dep,x}(x)dx = 1 - \left(\mathrm{erf}(A) + \frac{\exp\left(-A^2\right)-1}{\sqrt{\pi}A}\right), \tag{13}$$

where the parameter A in the error function is $(L^* - w^*)/\sqrt{12}Kn_D$.

Fig. 9(a) graphically shows the functional variation of $P_{dep,x}(x)$ with x in Eq. (12) with a dashed line, in contrast to the stepwise variation in Eq. (6). Note that particles, even located in the proximity of the side wall of column, do not have a deposition probability of 0.5; but behave with a deposition probability that gradually decreases with x until $x \le (L-w)/2$ and then goes up again with x up to 0.5 just like mirror image, referring to Fig. 9(a). The profile implies that particles located in the center between columns have the lowest but equal chance to deposit on either of the side walls, while particles displaced away from the center will deposit to any closer column wall with higher probability, though they can still deposit to the opposite wall with lower (but non-zero) probability. This figure sounds more realistic, taking into consideration the random nature of diffusive motion and its potential role in the probability.

Similarly, Fig. 9(b) highlights the variation of the resulting P_{dep} with Kn_D obtained by Eqs. (12-13), in comparison with that obtained by Eqs. (6) and (7). Clearly the assumption of a constant-distance random walk for all particles overestimates the average wall-deposition probability P_{dep} particularly when $\log Kn_D \ge 0$. It is interesting to reconfirm that the prediction of the first model using Eq. (10) becomes unrealistic when $\log Kn_D \ge 0$ as marked with B in Fig. 5(b). For example, Eq. (10) predicts the appearance of dendrites in the whole range of χ_F if $\log Kn_D \ge 1$ (see the upper dotted line in Fig. 5(b)). We speculated that this prediction bias toward the dendritic structure might be associated with the overestimation of P_{dep} in Fig. 9(b).

Thus, substituting Eqs. (13) and (9) to Eq. (5), the modified model equation is obtained as

$$\chi_F^{0.5} = C_1'' \ln\left(\mathrm{erf(B)} + \frac{\exp\left(-B^2\right)-1}{\sqrt{\pi}B}\right), \tag{14}$$

where B is C_2''/Kn_D. The two constants $C_1''$and C_2'' are determined by fitting the dataset representing structural transition boundary ($I =$ 0.4 or 0.7 in Fig. 5(b)) with Eq. (14) and listed in Table 1. The predicted boundary profile with $C_1''$and C_2'' for Case 2 in Table 1 is highlighted with the dashed line (- -) in Fig. 5(a) and (b), representing the dendritic-to-intermediate structural transition boundary. Whereas, the solid line in Fig. 5(a) and (b) shows the transition boundary obtained with the constants for Case 1 in Table 1. It is noteworthy that even with constant values of $C_1''$and C_2'', the boundaries of structural transitions are well predicted throughout the entire deposition condition range of this study.

4.3. Simplification of model equation and validation

In this section, Eq. (14) is simplified to gain an insight into functional relation of the Kn_D and χ_F on the transition boundary. Since the complexity arises from the logarithmic term in Eq. (14), two limiting conditions of the parameter B are considered as follows.

When $\mathrm{B} \ll 1$, the $\mathrm{erf(B)}$ and $\exp(-B^2)$ can be approximated to the first order upon Taylor series expansion, resulting in $2(B - B^3/3)/\sqrt{\pi}$ and $(1 - B^2)$, respectively. The both terms are substituted into Eq. (14) to be arranged as

$$\chi_F^{0.5} \cong C_1'' \ln\left(\frac{2}{\sqrt{\pi}}\left(B - \frac{B^3}{3}\right) + \frac{\left(1-B^2\right)-1}{\sqrt{\pi}B}\right) \cong C_1'' \ln\left(\frac{\mathrm{B}}{\sqrt{\pi}}\right) \tag{15}$$

On the other hand, if $\mathrm{B} \gg 1$, then the $\mathrm{erf(B)}$ is approaching 1, and $\exp(-B^2)$ will vanish. So, under this approximation, Eq. (14) is now expressed as $\chi_F^{0.5} \cong C_1'' \ln(1 - 1/\sqrt{\pi}B)$, which is further simplified using the Taylor series expansion of $\ln(1-\mathrm{x}) = -x - x^2/2 + O(x^3)$ as

$$\chi_F^{0.5} \cong -\frac{C_1''}{\sqrt{\pi}B} \tag{16}$$

Equations (15-16) are rearranged in terms of Kn_D and χ_F to yield the simplified model equation as

$$Kn_D = \begin{cases} C_1 \exp\left(C_2 \chi_F^{0.5}\right) & \left(Kn_D > 10^0 \text{ or } 10^{-0.5}\right) \\ C_3 \chi_F^{0.5} & \left(Kn_D \le 10^0 \text{ or } 10^{-0.5}\right) \end{cases}. \tag{17}$$

where the C_1, C_2, and C_3 are all constant and two sets of them are listed for Case 1 and 2 in Table 1. Actually, either the dotted line or

solid line in Fig. 5 is likely divided to a curved section upon high Kn_D and a linear section in low Kn_D. Since Fig. 5 is a log-log plot, the curved section of each boundary is expressed by the upper equation in Eq. (17), while the linear section is done by the lower equation.

Given a deposition condition in terms of (Kn_D, χ_F), for instance, if dendritic structure is of interest, one can start the prediction from collecting the three constants for Case 2 in Table 1 and then check if $Kn_D > 0.28\exp(7.69\chi_F^{0.5})$ when $Kn_D > 10^0$ or $Kn_D > 6.82\chi_F^{0.5}$ when $Kn_D \leq 10^0$. If so, one may predict the formation of dendritic structure. On the contrary, compact structure, corresponding to Case 1, will form if $Kn_D < 0.1\exp(2.27\chi_F^{0.5})$ when $Kn_D > 10^{-0.5}$ or $Kn_D < 0.68\chi_F^{0.5}$ when $Kn_D \leq 10^{-0.5}$. Deposit will have intermediate structure if the above conditions are not met altogether.

Peclet number (Pe), which is relevant to transport phenomena in continuum regime, is defined as a ratio of advective transport rate to diffusive transport rate of particles, so can be expressed in terms of Kn_D and χ_F as $Pe \equiv Kn_D^{-1}\chi_F^{0.5}$ (Lindquist et al., 2014). Li et al. (2009) reported through on-lattice MC simulation that as Pe increases, the fractal dimension of particle deposit initially increases and then levels off around 3 upon $Pe \geq 10^{-0.4}$, resulting in a compact structure. In their on-lattice MC simulation, a particle located in a cell of simulation lattice was allowed to move by diffusion to a neighboring cell for Δt. Since the cell-to-cell distance was equal to particle diameter in their study, the diffusive displacement l_{diff} in our study is now $2r_p$, which results in $Kn_D(\equiv l_{mfp}/r_p = l_{diff}/\sqrt{6}r_p) \cong 10^{-0.1}$. Next, recalling that their structural transition started from $Pe = 10^{-0.4}$, the corresponding χ_F is calculated to be 10^{-1} by substituting the two values into the foregoing expression $Pe \equiv Kn_D^{-1}\chi_F^{0.5}$. Interestingly, the condition of $Kn_D = 10^{-0.1}$ and $\chi_F = 10^{-1}$ indicates from Fig. 5 that their deposit structure has just started to transit from dendritic structure toward compact structure, staying around the intermediate structure between the dashed and solid lines. This is in reasonable agreement with their finding.

Referring to another on-lattice MC simulation result by Castillo et al. (2014), the dendritic structure was formed at $Pe = 10^{-1}$ corresponding to ($Kn_D = 10^{-0.1}$, $\chi_F = 10^{-2.2}$), while the compact structure was found at $Pe = 10^2$, i.e., ($Kn_D = 10^{-0.1}$, $\chi_F = 10^{3.8}$). Consistent with their findings, the first condition lies above the dashed line in Fig. 5, ensuring the dendritic structure, and the second condition is in red region, right of the solid line, representing the compact structure. The two experimental studies (Thimsen & Biswas, 2007; Thimsen et al., 2008) that showed SEM images of dendritic structures in Fig. 2 were used to further test the present criteria for prediction of deposit structure. Based on the literature, the relevant conditions are expressed as ($Kn_D = 10^{1.7}$, $\chi_F = 10^{-1.6}$) and ($Kn_D = 10^{1.5}$, $\chi_F = 10^{-0.6}$). Again one may confirm that the two conditions are safely in the blue region of Fig. 5(b) corresponding to the appearance of dendrites. Lastly it should be noted that there are very limited experimental literatures reporting the structural characteristics in connection with deposition condition, even for compact deposits. This is why the overall images of simulated deposits were qualitatively compared with the SEM images, though the overall porosity was directly compared with existing simulation data.

5. Conclusions

The purpose of this study is to provide a guidance for understanding structural change of nanoparticle deposits depending on the deposition conditions. The off-lattice MC simulation has been performed to produce various structures of nanoparticle deposits on a largest deposition substrate with $1000r_p \times 1000r_p$. The deposition conditions are expressed in terms of diffusive Knudsen number (Kn_D) and dimensionless translational energy (χ_F), and cover a wide range of the diffusion and advection of particles with Kn_D: $10^{-1.5}$–$10^{1.5}$ and χ_F: 10^{-3}–10^{3}. In contrast to compact structure that is relatively simple to analyze, little is known about dendritic structure comprising multiple dendrites even for its structural characteristics. With newly proposed concept of local porosity along the vertical prisms, we successfully visualized the distinct characteristics of deposit structures. Employing the spatial autocorrelation index I, deposit structures were quantitatively classified into dendritic, intermediate (transitional), and compact structures for the first time, e.g., with reference to $I > 0.7, 0.4 < I < 0.7,$ and $I < 0.4$, respectively. Also we provided a new contour plot of the index I as well as the overall porosity as a function of Kn_D and χ_F, plus simultaneously displaying the observed distinctive structure among the three microstructures with different symbols. Lastly, two versions of mathematical model equations were developed to predict a specific microstructure of deposit between the dendritic, intermediate, and compact structures based on Kn_D and χ_F and reasonably validated with existing simulation and experimental studies, for the first time.

Declaration of competing interest

The authors declare that they have no known competing financial interests or personal relationships that could have appeared to influence the work reported in this paper.

Acknowledgements

This work was supported by the National Research Foundation of Korea (NRF) (No. 2020R1A2C201163412); and also by Samsung Electronics DS Industry-University Cooperation Center.

Appendix A. Supplementary data

Supplementary data to this article can be found online at https://doi.org/10.1016/j.jaerosci.2021.105876.

Appendix. Spatial autocorrelation index

The spatial autocorrelation index, often known as Moran's I, measures the degree of correlation between variables distributed in space. Equation (A1) is the most commonly used formula of Moran's I (Zhang & Lin, 2007).

$$I = \frac{N}{W} \frac{\sum_i \sum_j w_{ij}(x_i - \bar{x})(x_j - \bar{x})}{\sum_i (x_i - \bar{x})^2}, \tag{A1}$$

where N is the number of lattice points used in the analysis; i and j are the lattice ID indexes varying from 1 to 250,000 in this study; x_i and x_j are actually the local porosity contour data displayed on a horizontal plane; $\bar{x}$ is the average value; w_{ij} is the weight between the i and j lattice points; and W is the sum of w_{ij} ($W = \sum_i \sum_j w_{ij}$). The weight (w_{ij}) was set to 1 for the four neighboring lattices (up and down, left and right) directly adjacent each other and 0 for all other lattices. The resulting value of I varies according to the resolution of lattice system (Qi & Wu, 1996), for example, a coarse lattice tends to reduce I values, while a too dense lattice if used can divide a single particle into several pieces so that can increase I value too much. Therefore, in this study, particle diameter (d_p) was selected as the lattice size, which is actually the same as that of the local porosity contours discussed in Section 3.2.

References

Bhattacharya, S., & Gubbins, K. E. (2006). Fast method for computing pore size distributions of model materials. *Langmuir, 22*, 7726–7731. https://doi.org/10.1021/la052651k

Castillo, J. L., Martin, S., Rodriguez-Perez, D., Perea, A., & Garcia-Ybarra, P. L. (2014). Morphology and nanostructure of granular materials built from nanoparticles. *KONA Powder and Particle Journal, 31*, 214–233. https://doi.org/10.14356/kona.2014012

Cherevko, S., & Chung, C. (2011). Direct electrodeposition of nanoporous gold with controlled multimodal pore size distribution. *Electrochemistry Communications, 13*(1), 16–19. https://doi.org/10.1016/j.elecom.2010.11.001

Choi, Y., Kim, N., Park, J., & Lee, W. (2010). Influences of thickness-uniformity and surface morphology on the electrical and optical properties of sputtered CdTe thin films for large-area II–VI semiconductor heterostructured solar cells. *Materials Science and Engineering: B, 171*(1), 73–78. https://doi.org/10.1016/j.mseb.2010.03.072

Elmøe, T. D., Tricoli, A., Grunwaldt, J., & Pratsinis, S. E. (2009). Filtration of nanoparticles: Evolution of cake structure and pressure-drop. *Journal of Aerosol Science, 40*(11), 965–981. https://doi.org/10.1016/j.jaerosci.2009.09.002

Fan, J., Tang, X., & Zhao, Y. (2004). Water contact angles of vertically aligned Si nanorod arrays. *Nanotechnology, 15*(5), 501–504. https://doi.org/10.1088/0957-4484/15/5/017

Friedlander, S. K. (2000). *Smoke, dust, and haze* (2nd ed.). Oxford Univ. Press.

Gao, L., Guo, H., Wei, L., Li, C., Gong, S., & Xu, H. (2015). Microstructure and mechanical properties of yttria stabilized zirconia coatings prepared by plasma spray physical vapor deposition. *Ceramics International, 41*(7), 8305–8311. https://doi.org/10.1016/j.ceramint.2015.02.141

Gao, W., Wang, Y., Zhang, H., Guo, B., Zheng, C., Guo, J., Gao, X., & Yu, A. (2020). A numerical investigation of the effect of dust layer on particle migration in an electrostatic precipitator. *Aerosol and Air Quality Research, 20*(1), 166–179. https://doi.org/10.4209/aaqr.2019.11.0609

Harris, M., Bowden, M., & Macleod, H. A. (1984). Refractive index variations in dielectric films having columnar microstructure. *Optics Communications, 51*(1), 29–32. https://doi.org/10.1016/0030-4018(84)90277-3

Hassani-Gangaraj, S. M., Moridi, A., & Guagliano, M. (2015). Critical review of corrosion protection by cold spray coatings. *Surface Engineering, 31*(11), 803–815. https://doi.org/10.1179/1743294415Y.0000000018

Hawkeye, M. M., & Brett, M. J. (2007). Glancing angle deposition: Fabrication, properties, and applications of micro- and nanostructured thin films. *Journal of Vacuum Science & Technology A, 25*(5), 1317–1335. https://doi.org/10.1116/1.2764082

Hinds, W. C. (1999). *Aerosol technology*. Incorporated: John Wiley & Sons.

Hunt, B., Thajudeen, T., & Hogan, C. J. (2014). The single-fiber collision rate and filtration efficiency for nanoparticles I: The first-passage time calculation approach. *Aerosol Science and Technology, 48*(8), 875–885. https://doi.org/10.1080/02786826.2014.938798

Kasper, G., Schollmeier, S., & Meyer, J. (2010). Structure and density of deposits formed on filter fibers by inertial particle deposition and bounce. *Journal of Aerosol Science, 41*(12), 1167–1182. https://doi.org/10.1016/j.jaerosci.2010.08.006

Khedir, K. R., Kannarpady, G. K., Ryerson, C., & Biris, A. S. (2017). An outlook on tunable superhydrophobic nanostructural surfaces and their possible impact on ice mitigation. *Progress in Organic Coatings, 112*, 304–318. https://doi.org/10.1016/j.porgcoat.2017.05.019

Kim, J., Yang, H., Kim, S., Pikhitsa, P. V., Kim, H., Suh, J., Kim, T., Choi, M., Kim, D. S., & Han, B. (2006). Parallel patterning of nanoparticles via electrodynamic focusing of charged aerosols. *Nature Nanotechnology, 1*(2), 117–121. https://doi.org/10.1038/nnano.2006.94

Kleinhans, U., Wieland, C., Frandsen, F. J., & Spliethoff, H. (2018). Ash formation and deposition in coal and biomass fired combustion systems: Progress and challenges in the field of ash particle sticking and rebound behavior. *Progress in Energy and Combustion Science, 68*, 65–168. https://doi.org/10.1016/j.pecs.2018.02.001

Kovalev, O. B., & Gusarov, A. V. (2017). Modeling of granular packed beds, their statistical analyses and evaluation of effective thermal conductivity. *International Journal of Thermal Sciences, 114*, 327–341. https://doi.org/10.1016/j.ijthermalsci.2017.01.003

Kubo, M., Ishihara, Y., Mantani, Y., & Shimada, M. (2013). Evaluation of the factors that influence the fabrication of porous thin films by deposition of aerosol nanoparticles. *Chemical Engineering Journal, 232*, 221–227. https://doi.org/10.1016/j.cej.2013.07.097

Kulkarni, P., & Biswas, P. (2004). A brownian dynamics simulation to predict morphology of nanoparticle deposits in the presence of interparticle interactions. *Aerosol Science and Technology, 38*(6), 541–554. https://doi.org/10.1080/02786820490466747

Lee, J., & Hogan, C. J., Jr. (2021). Computational predictions of porosities, pore size distributions, and conductivities of aerosol deposited particulate films. *Powder Technology, 378*, 400–409. https://doi.org/10.1016/j.powtec.2020.09.078

Lindquist, G. J., Pui, D. Y. H., & Hogan, C. J. (2014). Porous particulate film deposition in the transition regime. *Journal of Aerosol Science, 74*, 42–51. https://doi.org/10.1016/j.jaerosci.2014.03.007

Li, Y., Vu, N., & Kim, A. S. (2009). 3-D Monte Carlo simulation of particle deposition on a permeable surface. *Desalination, 249*(1), 416–422. https://doi.org/10.1016/j.desal.2009.05.018

Mädler, L., Lall, A. A., & Friedlander, S. K. (2006). One-step aerosol synthesis of nanoparticle agglomerate films: Simulation of film porosity and thickness. *Nanotechnology, 17*(19), 4783–4795. https://doi.org/10.1088/0957-4484/17/19/001

Mädler, L., Roessler, A., Pratsinis, S. E., Sahm, T., Gurlo, A., Barsan, N., & Weimar, U. (2006). Direct formation of highly porous gas-sensing films by in situ thermophoretic deposition of flame-made Pt/SnO2 nanoparticles. *Sensors and Actuators B, 114*(1), 283–295. https://doi.org/10.1016/j.snb.2005.05.014

Mädler, L., Sheldon, K., & Friedlander. (2007). Transport of nanoparticles in gases: Overview and recent advances. *Aerosol and Air Quality Research, 7*(3), 304–342. https://doi.org/10.4209/aaqr.2007.03.0017

Moran, P. A. (1950). Notes on continuous stochastic phenomena. *Biometrika, 37*(1/2), 17–23. https://doi.org/10.2307/2332142

Morán, J., Yon, J., & Poux, A. (2020). Monte Carlo aggregation code (MCAC) Part 1: Fundamentals. *Journal of Colloid and Interface Science, 569*, 184–194. https://doi.org/10.1016/j.jcis.2020.02.039

Nasiri, N., Elmøe, T. D., Liu, Y., Qin, Q. H., & Tricoli, A. (2015). Self-assembly dynamics and accumulation mechanisms of ultra-fine nanoparticles. *Nanoscale, 7*(21), 9859–9867. https://doi.org/10.1039/C5NR00877H

Ortiz, T., Conde, C., Khan, T., & Hussain, B. (2017). Thickness uniformity and optical/structural evaluation of RF sputtered ZnO thin films for solar cell and other device applications. *Applied Physics A, 123*(4), 1–6. https://doi.org/10.1007/s00339-017-0909-2

Qi, Y., & Wu, J. (1996). Effects of changing spatial resolution on the results of landscape pattern analysis using spatial autocorrelation indices. *Landscape Ecology, 11*(1), 39–49. https://doi.org/10.1007/BF02087112

Rodríguez-Pérez, D., Castillo, J. L., & Antoranz, J. C. (2005). Relationship between particle deposit characteristics and the mechanism of particle arrival. *Physical Review E, 72*(2), Article 021403. https://doi.org/10.1103/PhysRevE.72.021403

Rodriguez-Perez, D., Castillo, J. L., & Antoranz, J. C. (2007). Density scaling laws for the structure of granular deposits. *Physical Review E, 76*(1), Article 011407. https://doi.org/10.1103/PhysRevE.76.011407

Strobel, R., & Pratsinis, S. E. (2007). Flame aerosol synthesis of smart nanostructured materials. *Journal of Materials Chemistry, 17*(45), 4743–4756. https://doi.org/10.1039/b711652g

Thimsen, E., & Biswas, P. (2007). Nanostructured photoactive films synthesized by a flame aerosol reactor. *AIChE Journal, 53*(7), 1727–1735. https://doi.org/10.1002/aic.11210

Thimsen, E., Rastgar, N., & Biswas, P. (2008). Nanostructured TiO2 films with controlled morphology synthesized in a single step Process: performance of dye-sensitized solar cells and photo watersplitting. *Journal of Physical Chemistry C, 112*(11), 4134–4140. https://doi.org/10.1021/jp710422f

Torquato, S. (2002). *Random heterogeneous materials: Microstructure and macroscopic properties*. Springer.

Tricoli, A., Graf, M., Mayer, F., Kuühne, S., Hierlemann, A., & Pratsinis, S. E. (2008). Micropatterning layers by flame aerosol deposition-annealing. *Advanced Materials, 20*(16), 3005–3010. https://doi.org/10.1002/adma.200701844

Tricoli, A., Nasiri, N., Chen, H., Wallerand, A. S., & Righettoni, M. (2016). Ultra-rapid synthesis of highly porous and robust hierarchical ZnO films for dye sensitized solar cells. *Solar Energy, 136*, 553–559. https://doi.org/10.1016/j.solener.2016.07.024

Veerapaneni, S., & Wiesner, M. R. (1994). Particle deposition on an infinitely permeable surface: Dependence of deposit morphology on particle size. *Journal of Colloid and Interface Science, 162*(1), 110–122. https://doi.org/10.1006/jcis.1994.1015

Zhang, T., & Lin, G. (2007). A decomposition of Moran's I for clustering detection. *Computational Statistics & Data Analysis, 51*(12), 6123–6137. https://doi.org/10.1016/j.csda.2006.12.032

Zhang, Y., Shuiqing, L., Deng, S., Yao, Q., & Stephen, D. T. (2012). Direct synthesis of nanostructured TiO2 films with controlled morphologies by stagnation swirl flames. *Journal of Aerosol Science, 44*, 71–82. https://doi.org/10.1016/j.jaerosci.2011.10.001